Impact of Inter-body Scattering on People Counting with Wi-Fi Sensing

Laurent Storrer*‡, Hasan Can Yildirim*†, Jérôme Louveaux†,
Philippe De Doncker*, Sofie Pollin‡, François Horlin*

*Université Libre de Bruxelles - †Université Catholique de Louvain - ‡Katholieke Universiteit Leuven
laurent.storrer@ulb.be, Hasan.Can.Yildirim@vub.be, jerome.louveaux@uclouvain.be,
sofie.pollin@kuleuven.be, {pdedonck,fhorlin}@ulb.ac.be

Abstract—We investigate the interactions between human bodies exposed to an incident electric field from a sensing-enabled Wi-Fi access point, to assess how it could affect people counting in the framework of Wi-Fi sensing. We model people with dieletric cylindrical shells with a thickness slightly higher than the electromagnetic skin depth. The electric field scattered by people is computed using the two-dimensional method of moments for electromagnetic scattering, accelerated using an iterative GMRES solver with Adaptive Cross Approximation and a block-Jacobi preconditionner. That scattered field is used to derive channel transfer functions that are combined to obtain a range-Doppler map. The presence of several ghost targets even in simple cases is highlighted, and could hinder people counting. When two people are aligned in front of the sensing-enabled Wi-Fi access point, the first blocking the line-of-sight of the second, it is shown that the field passing through the first person and reflected on the second person is sufficiently strong to detect it. We quantify the corresponding attenuation.

Index Terms—Wi-Fi sensing, Method of Moments, ghost targets, people counting.

I. INTRODUCTION

With the ongoing work of the 802.11 Task Group for WLAN sensing [1], remote monitoring with sensing-enabled Wi-Fi devices has drawn increasing attention. Indoor small scale applications of WLAN sensing consist of human activity classification [2], occupancy detection [3] and human movements tracking [4].

Larger scale WLAN sensing aims, among other topics, at monitoring groups of people and crowds. This can be achieved by means of Wi-Fi-based radars. In [5], the number of people in a crowd is counted by using a Naive Bayes classifier on the Doppler spectrum estimated by a Wi-Fi-based passive radar. In [6], groups of up to 20 people are counted through walls using a maximum likelihood estimation based on the RSSI measured by a Wi-Fi access point (AP). The channel state information (CSI) estimated by a Wi-Fi AP can also be used to count people, for example by extracting features from the CSI and feeding them to a Support Vector Machine (SVM) classifier.

However most of these approaches in the literature feed features from CSI or range-Doppler maps to classifiers without paying attention to the underlying interactions between the bodies to count. Indeed, when measuring echoes from several targets using a (passive) radar-based Wi-Fi-sensing device, high order multipath components (MPCs) can arise from the signal bouncing between people. One person can also drastically attenuate the echoes created by people located behind her, hindering their detection by the sensing device. Those phenomena can affect the counting of the number of people. Thus, even if the aforementioned counting approaches work in practice, it is worth to investigate those physical aspects. With this purpose in mind, we model the interactions between an incident electric field, emitted by a sensing-enabled Wi-Fi AP, and people using the two-dimensional method of moments for electromagnetic scattering [7], noted here as MoM.

Existing work available in the literature on human body response to electromagnetic waves focuses mainly on a single body. In [8], a single body is modeled as an infinite lossy dielectric cylinder and the MoM is applied to derive a channel model for a body area network, by computing the electric field scattered in response to an incident field from a current line located near the body. A combination of the finite element method (FEM) and the MoM is also used in [9] to compute assess the single body exposure by computing the average whole-body specific absorption rate (SAR) in the near-field of a GSM base station antenna. Various modeling software that compute the Radar Cross Section (RCS) and SAR are compared in [10], by taking into account the permittivity and conductivity of different parts of the body (tissues, muscles,...).

There is few available research on scattering by multiple bodies. Existing work on this subject uses analytical frameworks, mainly applied to propagation among trees: in [11], the fading caused by roadside trees on the signal of land mobile satellite channels is investigated. The author model the trees as finite dielectric cylinders, with randomly placed cylindrical branches and disk-shaped leaves randomly placed on the branches. They then compute an analytical expression of the scattered field by means of the Foldy-Lax's multiple scattering theory [12], [13]. The Foldy-Lax's theory is also used in [14] to model the propagation of waves among randomly placed trees modelled as cylinders using the infinite cylinder approximation (ICA), which is valid when "the length of the cylinder is much longer than the wavelength" [15].

Our work aims at extending the knowledge about multiple human bodies interactions by using the MoM, which

intrinsically enables a fine characterization of the diffraction phenomenon for multiple bodies, and is well suited to handle cylindrical objects. Our contributions are the following:

- Creating a multi-body MoM framework for channel simulations applicable to Wi-Fi-based sensing purposes. Bodies are modelled as dielectric cylindrical shells whose thickness is equal to the electromagnetic skin depth, with respect to the complex relative permittivity ε_r of the body computed by considering the body as a mixture of bones, muscles, fat, organs, blood, skin and humors. The multiple bodies are illuminated by a sensing-enabled Wi-Fi AP.
- Analyzing the presence of ghost targets that could affect the counting in a simple two-targets scenario, and determining the amplitude of those ghost targets.
- Quantifying the attenuation of targets located behind another target at Wi-Fi frequencies.

This article is structured as follows: in Section II, the human body model is presented, and the MoM is briefly explained, along with the techniques used to accelerate it. In Section III, the simulation results are presented: an analysis of ghost targets using the MoM is presented, and the attenuation of a target located behind another target is quantified. Section IV concludes the article.

II. MODEL

A. Human body modeling

The human body is modelled as a mixture of bones, muscles, fat, organs, blood, skin and humors whose respective relative permittivity and conductivity are provided by [16]. The resulting total relative permeability ε_r and conductivity σ are shown as a function of the carrier frequency in Fig. 1.
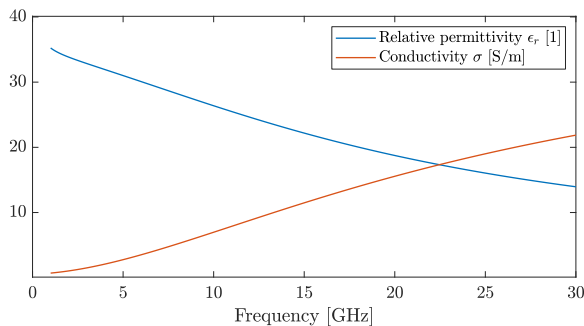

Fig. 1. Relative permeability and conductivity of the modelled body

The human body can be modelled as an infinitely high dielectric cylinder along the z dimension, following the aforementioned infinite cylinder approximation [14], [15], with a radius $r = 0.2$ m. The cross section of each cylinder in the xy plane is discretized into circular cells whose side length is $\Delta = \lambda_{in}/5$, where λ_{in} is the wavelength inside the dielectric [7]. Equivalently, the body can be modelled as a dielectric cylindrical shell whose height is infinite and whose thickness is equal to the electromagnetic skin depth δ plus two discretization steps Δ. Both are equivalent since δ is the characteristic distance of the exponential attenuation of the total field inside the dielectric. The field is thus significantly attenuated beyond that distance in the dielectric. A comparison between the scattering width, *i.e.* the two-dimensional radar cross section, of the cylinder and of cylindrical shells with different thicknesses at 2.45 GHz is provided in Fig. 2, as a function of the polar angle Φ. This shows the equivalence between the dielectric cylinder and the cylindrical shell of thickness δ, $\delta + \Delta$, or $\delta + 2\Delta$. The shell of thickness $\delta + 2\Delta$ is chosen because its scattering width is closer from the scattering width of the cylinder at higher polar angles.
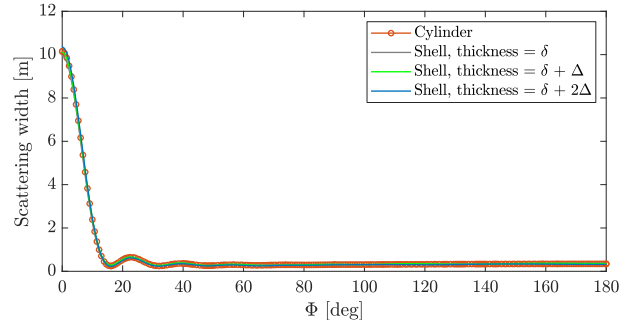

Fig. 2. Scattering width of a dielectric cylinder and cylindrical shells of various thicknesses at 2.45 GHz

The set of (x, y) points in space belonging to all the different bodies is noted $\mathcal{B}$.

B. MoM and transfer function

We note the frequency-dependent component of a vertically polarized incident field at any point (x, y) in space as $E^i_{(x,y)}(f)$, emitted by the sensing device, where f is the frequency. By defining $d_{\text{TX}} = \sqrt{(x - x_{\text{TX}})^2 + (y - y_{\text{TX}})^2}$ as the distance between a point and the coordinates $(x_{\text{TX}}, y_{\text{TX}})$ of the transmitting antenna TX, the incident field is considered to be a cylindrical wave expressed as:

$$E^i_{(x,y)}(f) = \frac{E_0}{\sqrt{d_{\text{TX}}/d_0}} e^{-j2\pi f d_{\text{TX}}/c}, \qquad (1)$$

where E_0 is a reference field, d_0 a reference distance and c is the speed of light in vacuum.

The field scattered by the objects is noted $E^s_{(x,y)}(f)$. The total field is $E_{(x,y)}(f) = E^i_{(x,y)}(f) + E^s_{(x,y)}(f)$. We consider the vectors $\boldsymbol{E}$ and $\boldsymbol{E^i}$ of the total fields and incident fields, respectively, in the points (x, y) belonging to the set of discretization cells of the bodies only, *i.e.* the points $(x, y) \in \mathcal{B}$. Using the MoM formalism, the link between the incident field and the total field in all bodies can be expressed by a linear system of equations [7]:

$$\boldsymbol{C}\boldsymbol{E} = \boldsymbol{E^i}. \qquad (2)$$

The entries of matrix $\boldsymbol{C}$ are obtained from the Maxwell's equations for each discrete cell in the cross section of bodies. This system of equations is valid for an arbitrary number of bodies simultaneously: the diagonal blocks of $\boldsymbol{C}$ account for

the interactions between cells of the same body, while the non-diagonal blocks account for the interactions between cells of different bodies [7]. In other words, the interactions between all bodies illuminated by the incident field are modelled with one single system of equations. Eq. (2) has to be solved for E to find the total field in each cell of the bodies. Then, using Maxwell's equations again, E is used to obtain the scattered field $E^s_{(x,y)}(f)$ outside the bodies, *i.e.* at the points $(x,y) \notin \mathcal{B}$.

The incident, scattered and total fields are frequency-dependent. Hence, the channel transfer function (CTF) can be derived by running the MoM at Q frequencies $f_q = f_c + q\frac{B}{Q}$ on a bandwidth B around a carrier frequency f_c, with $q \in \mathbb{Z} \cap [-\frac{Q}{2}, \frac{Q}{2} - 1]$. We assume that the incident field is perfectly cancelled at the receiving antenna RX. The CTF is usually expressed as the ratio of the voltages at RX and TX. Here we compute a normalized CTF H, expressed at each frequency f_q as

$$H(f_q) = \frac{E^s_{\mathrm{RX}}(f_q)}{E_0}, \tag{3}$$

where E^s_{RX} is the scattered field at RX, due to all the bodies. Hence, the CTF H derived from the MoM accounts for the interactions of all the bodies at once, for an arbitrary number of bodies. The normalized channel impulse response (CIR) $h(\tau)$ as a function of the propagation delay τ can be obtained by an inverse Fast Fourier Transform (IFFT). Equivalently, h can be expressed as a function of the distance $d = c\tau/2$ of the bodies, hence as $h(d)$. This CIR contains all echoes created by scattering on the multiple bodies, including MPCs between the bodies, since all interactions are contained in matrix C.

Evaluating $h(\tau)$ at N slow time instants spaced by a time T and computing a Fast Fourier Transform (FFT) across the slow time reveals the Doppler frequency shift caused by the movements of bodies and yields the usual range-Doppler map (RDM), noted by D here. The speed v of a bodies is estimated from its Doppler frequency f_D as $\hat{v} = \lambda f_D/2$, where $\lambda = c/f_c$ is the wavelength in vacuum.

C. MoM acceleration

In (2), there is one equation per discretization cell, hence the resolution of the system is computationally intensive due to the high number of equations. It is accelerated by exploiting the block structure of C. A generalized minimal residual (GMRES) iterative solver is used [17], where the matrix-vector product is implemented block by block. Non-diagonal blocks have a low-rank structure and can be compressed using Adaptive Cross Approximation (ACA) [18]. This does not require to compute the full block and significantly accelerates the matrix-vector product for these blocks [19]. Moreover, C is symmetrical, meaning that only the ACA of the non-diagonal blocks of the upper triangular part of the matrix need to be computed, and can be reused for the lower triangular part.

A block-Jacobi preconditioner is used to improve the conditioning of the system, leading to a faster convergence of GMRES [20]. It requires the computation of the inverse of the diagonal blocks of C. This is done by computing their LU factorization. The diagonal blocks of C, corresponding to

the interactions between cells of the same body, are identical since all simulated bodies are identical. Hence, only one LU factorization needs to be computed, and can be reused for the other diagonal blocks.

III. RESULTS

A. Ghost targets

First, we show that ghost targets can arise unexpectedly even in simple cases. We consider the case A illustrated in Fig. 3, where two targets, T1 and T2, move on a horizontal line w.r.t. a sensing-enabled Wi-Fi AP acting as monostatic TX/RX. The targets are located on each side of TX/RX. The centers of T1 and T2 are d_1 and d_2 meters away from the AP, while their speeds, v_1 and v_2, are relative to TX/RX. The carrier frequency is $f_c = 2.45$ GHz. The normalized CTF is computed on $Q = 16$ different frequencies spanning a bandwidth $B = 100$ MHz, in the range of the available bandwidth with the latest and in-development Wi-Fi standards. The number of points of the Doppler FFT is $N = 32$, and the slow time instants are spaced by a time $T = 5$ ms. At 2.45 GHz, it gives a speed resolution of 0.38 m/s. The value of Q and N are chosen small for computation time considerations, since the MoM is run for each frequency f_q for each slow time instant. However it does not affect the conclusions of the analysis. The obtained RDM is displayed in Fig. 4.
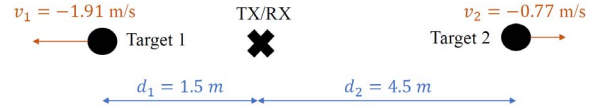

Fig. 3. Case A for ghost targets. The sign of the Doppler shift w.r.t. TX/RX is included in the scheme.
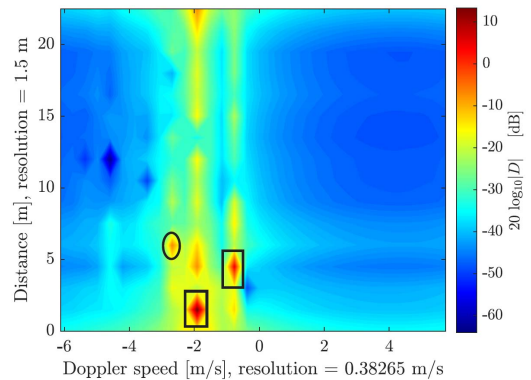

Fig. 4. RDM for Case A with true targets (black rectangles) and ghost targets (black circles).

The returns from both targets are highlighted with a black rectangle. The targets present leakage along the range axis, which is expected since all of their discretization cells are not located at an integer multiple of the range resolution. They do not exhibit speed/Doppler leakage since their speeds were set to integer multiples of the speed resolution. It can be seen that there is one ghost target, highlighted by a black ellipse.

It is located at a range $d_1 + d_2$, and it has a speed of $v_1 + v_2$. Its amplitude is less than 10 dB lower than the second target amplitude. This ghost target could thus mislead a counting algorithm. However its presence could have been predicted by a simple ray tracer with a two-order bounce model, that is why a more advanced case is investigated, exploiting the potential of the MoM.

In the second case, named Case B, T1 and T2 are on the same side of TX/RX, as illustrated in Fig. 5. T1 is the closest to the AP. T2 is the farthest from the AP and is totally masked by T1. The RDM yielded by the MoM is displayed in Fig. 6.
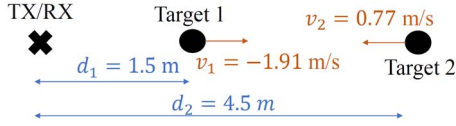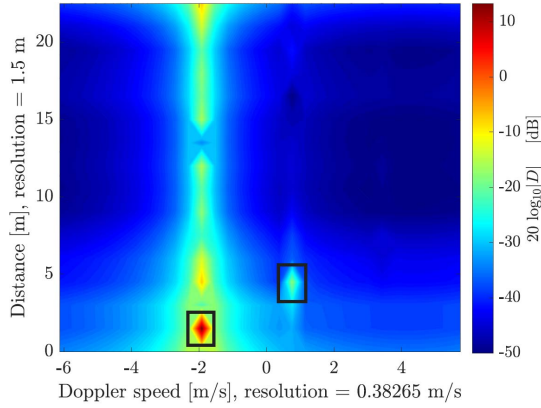

Fig. 5. Case B for ghost targets

Fig. 6. RDM for Case B with true targets (black rectangles)

It can be noticed that T2 it is still detectable, yet attenuated. No ghost target is noticed here. Indeed, the attenuation of the target echo from T2 due to the masking by T1 is already significant, hence higher order MPCs occuring between T1 and T2 are too much attenuated to be detectable. This is positive since in that situation a counting would not be hindered.

Variations of cases A and B were analyzed to obtain a model of those ghost targets depending on the position of the targets w.r.t. TX/RX. They are divided into two cases. By defining $\boldsymbol{x}$, $\boldsymbol{x_1}$ and $\boldsymbol{x_2}$ as the position vectors on a line of TX/RX, T1, and T2, respectively,

$$\eta = (\boldsymbol{x} - \boldsymbol{x_1}) \cdot (\boldsymbol{x} - \boldsymbol{x_2}) \qquad (4)$$

can be computed. If $\eta < 0$, the targets are not on the same side of TX/RX. This corresponds to case A. If $\eta > 0$, both targets are on the same side of TX/RX. This corresponds to case B. A model summarizing the ghost detection and its range-Doppler characteristics for each case is presented in Table I. It can be noticed that in case A, a second ghost is present at the same range and speed as the first one, hence superimposed with it. The presence of this ghost can be explained via the physical development given herebelow.

	Case A: $\eta < 0$		Case B: $\eta > 0$
Ghost n°	1	2	
$d_{\text{ghost}} =$	$d_1 + d_2$	$d_1 + d_2$	Not detectable
$v_{\text{ghost}} =$	$v_1 + v_2$	$v_1 + v_2$	

In case A, the ghosts can be explained physically by the higher order MPCs occuring between T1 and T2, including relative Doppler shifts between them. The physical process behind the first ghost in Case A (Fig. 3) can be decomposed as follows:

1) The incident field from TX/RX propagates to T1.
2) T1 perceives it shifted by a Doppler frequency $f_{D_1}/2 = v_1/\lambda$, with the sign w.r.t. TX/RX included.
3) T1 reemits a scattered field in reaction to the incident field. The scattered field is shifted by $f_{D_1}/2$ and arrives on T2.
4) T2 perceives it shifted by the relative Doppler between T1 and T2, $f_{D_2}/2 + f_{D_1}/2$. There is a $+$ sign because the speeds are relative towards TX/RX so they have an opposite sign convention.
5) T2 reemits a field which has a total shift of $f_{D_1}/2 + f_{D_1}/2 + f_{D_2}/2$.
6) This field arrives at TX/RX, which perceives it with an extra shift of $f_{D_2}/2$.

The field travelled a total distance $2(d_1 + d_2)$ corresponding to a range $d_{\text{ghost}} = d_1 + d_2$ w.r.t. TX/RX, with a total Doppler shift of $f_{D_1}/2 + f_{D_1}/2 + f_{D_2}/2 + f_{D_2}/2 = f_{D_1} + f_{D_2}$, corresponding to a speed $v_1 + v_2$. The same physical process also happens with the first echo on T2, giving rise to a second ghost travelling the same distance with the same total Doppler shift as the first one. Both ghosts are thus superimposed.

For case B (Fig. 5), interactions between T1 and T2 similar to case A are present, however the attenuation through T1 is significant enough to prevent ghosts from appearing in the RDM.

Ghost targets created by higher order MPCs on the surrounding elements (walls, ground, furnitures,...) are a well known problem. However, here, we highlight ghosts resulting only from target-to-target interactions and analyze their physical origin. On the other hand, we highlight the fact that in a case of total target masking, higher order MPCs are too much attenuated to create ghosts at the studied frequency (2.45 GHz). However, considering partial masking only and scaling this phenomenon to higher numbers of targets would increase the number of ghosts resulting from target-to-target interactions and may yield counting results being far from reality.

B. Shadow zone

Aside from the ghost targets, Scenario B (Fig. 5) can be investigated further. The total field $E_{(x,y)}(f)$ computed by the MoM for one slow time instant in the xy plane when only T1

is present is displayed in Fig. 7. TX/RX is represented by a black cross on the left, while T1 is represented by the black circle. It can be noticed that a region of low field values is present behind T1, in blue on the plot. We name it the *shadow zone* of T1. If T2 would be present, it would thus be located in this shadow zone and attenuated.
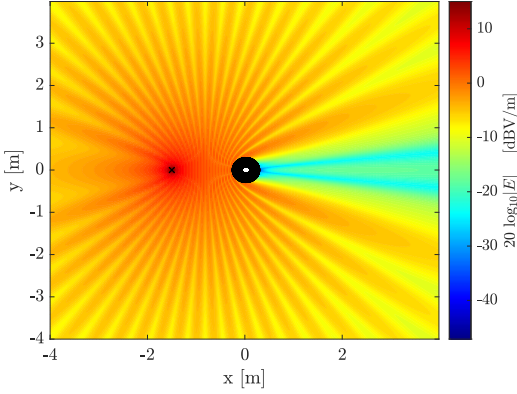

Fig. 7. Total field $E_{(x,y)}(f)$ outside the body, to illustrate of the shadow zone. TX/RX is represented by a black cross on the left, while T1 is represented by the black circle.

However on the RDM in Fig. 6 where both targets were present, T2 was still noticeable, meaning that the shadow zone created by T1 does not mask totally T2. To quantify the attenuation created by that shadow zone, we compute a shadow zone ratio γ as a function of the distance between T1 and T2, $d_2 - d_1$, *i.e.* as function of the position of T2 in the shadow zone.

$$\gamma(d_2 - d_1) = \frac{|h(d_2)|_{\text{shadowed}}}{|h(d_2)|_{\text{not shadowed}}} \quad (5)$$

so the ratio of the CIR coefficient modulus at T2's range d_2 when both T1 and T2 are present and the CIR coefficient modulus at T2's range when only T2 is present. The simulation is repeated for different ranges d_2 to assess the attenuation via γ. The way γ is defined ensures that it measures only the attenuation of T2 due to the presence of T1 and not the effect of the field propagation distance. The concept of the shadow zone ratio is illustrated on the CIR in Fig. 8, with the CIRs for the case with both targets and with T2 only, respectively: the first vertical dotted line marks the range d_1 of T1 while the second marks the range d_2 of T2. γ is the ratio between the red and the green dots located at the range d_2.

The graph of γ as a function of the distance between T1 and T2, $d_2 - d_1$ is given in Fig. 9. The simulation is performed at $f_c = 2.45$ GHz and with a very large bandwidth $B = 2$ GHz to reduce the parasitic effect of range-axis leakage on the value of γ: indeed since the range-axis leakage can vary with the range of T2, it can create unwanted variations of $|h(d_2)|$, pertubating the computation of γ. As expected, γ is very low for short values of $d_2 - d_1$, since the attenuation of T2 due to T1 is the largest when T2 is close from T1. At 0.45 m from T1, $\gamma = 0.034$, meaning that 3.4 % of the energy of T2, *i.e.* the energy of T2 that would be detected if T1 was not present,
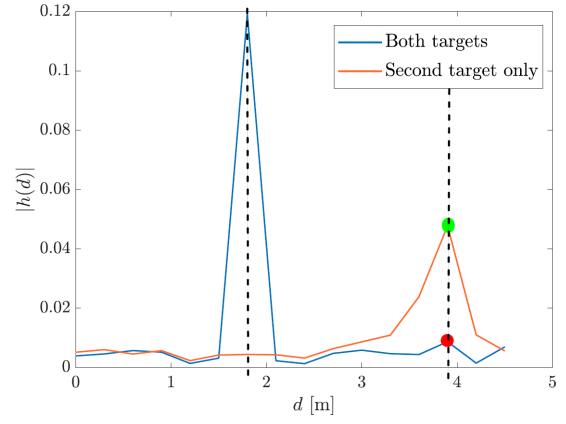

Fig. 8. CIR $h(d)$ to illustrate the shadow zone ratio γ concept. The first vertical dotted line marks the range d_1 of T1 while the second marks the range d_2 of T2. The shadow zone ratio for a given d_2 is the ratio between the red and the green dot.
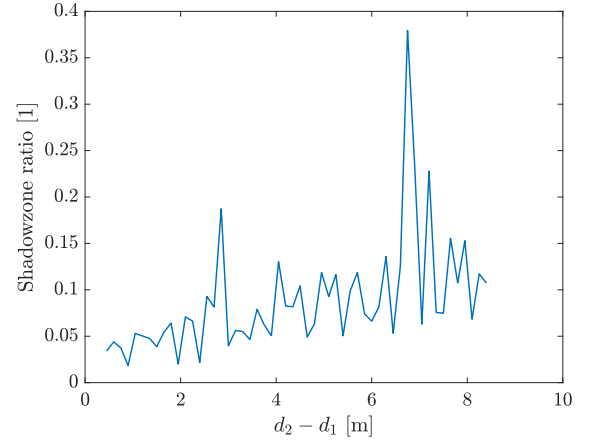

Fig. 9. Shadow zone ratio γ

comes back to TX/RX. It means that T2 is strongly attenuated but still detectable, confirming the fact that T2 is not totally shadowed by T1. γ presents a very slow increasing tendency with $d_2 - d_1$, reaching values around 0.1 at 8 m from T1. This means that the shadow zone from T1 is still applying a heavy attenuation effect on targets located in it, even several meters away. It would thus require a long distance between the targets to get rid of its effect. However, as already mentioned and noticed on Fig. 6, even with this strong attenuation the second target is still detectable.

It can also be noticed that γ presents sawtooth variations and strong peaks instead of increasing smoothly. This can explained by looking at the scattered field $E^s_{(x,y)}(f)$ when both targets are present, and zooming on the area close to T1 and T2, as shown in Fig. 10[1]. TX/RX is represented by a black cross on the left, while T1 and T2 are represented by the black ellipses (*i.e.* the circles distorted by the scale of the plot). Interestingly, $E^s_{(x,y)}(f)$ between T1 and T2 exhibits

---

[1]On that plot, T2 was set close to T1 in order to zoom on the area of interest and plot the scattered field with a high granularity.

an oscillatory behaviour corresponding to a stationary wave, due to the sum of all high order MPCs bouncing between T1 and T2 and interfering with each other. The amplitude peaks of γ correspond to strong constructive interferences, allowing T2 to be detected with high amplitude at certain critical positions. γ, that depends on $E^s_{(x,y)}(f)$ through $h(d)$, is computed for an increasing distance between T1 and T2 with a fixed step that needs to be equal to or higher than the range resolution. However, even with a bandwidth of 2 GHz, the range resolution is not high enough to sample this oscillatory behaviour properly. Hence γ samples those oscillations too slow, resulting in the sawtooth variations. Nevertheless, these variations do not prevent the analysis of the global shape of γ.
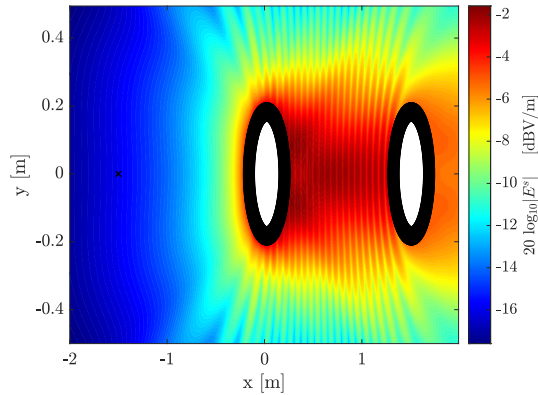

Fig. 10. Zoom on the scattered field $E^s_{(x,y)}(f)$, outside the bodies, in Scenario B, to highlight its oscillatory behaviour. TX/RX is represented by a black cross on the left, while T1 and T2 are represented by the black ellipses (*i.e.* the circles distorted by the scale of the plot).

IV. CONCLUSION

We presented a human body model suitable to compute the electric field scattered by multiple human bodies in response to an incident field from a sensing-enabled Wi-Fi access point via an accelerated Method-of-Moments. This was used to study the interactions occurring among the bodies. The presence of ghost targets able to hinder the counting of people was investigated, and the physical phenomenon behind them was explained. The attenuation caused by a first body on a second body located behind it was also quantified.

V. ACKNOWLEDGEMENTS

REFERENCES

[1] IEEE 802.11, "Wi-Fi sensing," 2019, Last consultation: February 2020. [Online]. Available: https://mentor.ieee.org/802.11/documents?is_dcn=DCN%2C%20Title%2C%20Author%20or%20Affiliation&is_group=SENS

[2] W. Li, B. Tan, and R. J. Piechocki, "Wifi-based passive sensing system for human presence and activity event classification," *IET Wireless Sensor Systems*, vol. 8, no. 6, pp. 276–283, Dec. 2018.

[3] C. Tang, W. Li, S. Vishwakarma, K. Chetty, S. Julier, and K. Woodbridge, "Occupancy detection and people counting using wifi passive radar," in *2020 IEEE Radar Conference (RadarConf20)*. IEEE, 2020, pp. 1–6.

[4] L. Storrer, H. C. Yildirim, M. Crauwels, E. I. P. Copa, S. Pollin, J. Louveaux, P. De Doncker, and F. Horlin, "Indoor tracking of multiple individuals with an 802.11 ax wi-fi-based multi-antenna passive radar," *IEEE Sensors Journal*, vol. 21, no. 18, pp. 20 462–20 474, Sept. 2021.

[5] S. Di Domenico, G. Pecoraro, E. Cianca, and M. De Sanctis, "Trained-once device-free crowd counting and occupancy estimation using wifi: A doppler spectrum based approach," in *2016 IEEE 12th International Conference on Wireless and Mobile Computing, Networking and Communications (WiMob)*. IEEE, 2016, pp. 1–8.

[6] S. Depatla and Y. Mostofi, "Crowd counting through walls using wifi," in *2018 IEEE international conference on pervasive computing and communications (PerCom)*. IEEE, 2018, pp. 1–10.

[7] J. Richmond, "Scattering by a dielectric cylinder of arbitrary cross section shape," *IEEE Transactions on Antennas and Propagation*, vol. 13, no. 3, pp. 334–341, May 1965.

[8] A. M. Eid and J. W. Wallace, "Accurate modeling of body area network channels using surface-based method of moments," *IEEE Transactions on Antennas and Propagation*, vol. 59, no. 8, pp. 3022–3030, Aug. 2011.

[9] F. J. Meyer, D. B. Davidson, U. Jakobus, and M. A. Stuchly, "Human exposure assessment in the near field of gsm base-station antennas using a hybrid finite element/method of moments technique," *IEEE Transactions on Biomedical Engineering*, vol. 50, no. 2, pp. 224–233, Feb. 2003.

[10] R. Neely, K. Naishadham, A. Sharma, and K. Bing, "Electromagnetic human body modeling with physiological motion for radar applications," in *2012 IEEE Radar Conference*. IEEE, 2012, pp. 0818–0823.

[11] M. Cheffena and F. Pérez-Fontán, "Channel simulator for land mobile satellite channel along roadside trees," *IEEE Transactions on antennas and propagation*, vol. 59, no. 5, pp. 1699–1706, May 2011.

[12] L. L. Foldy, "The multiple scattering of waves. i. general theory of isotropic scattering by randomly distributed scatterers," *Phys. Rev.*, vol. 67, pp. 107–119, Feb. 1945. [Online]. Available: https://link.aps.org/doi/10.1103/PhysRev.67.107

[13] M. Lax, "Multiple scattering of waves," *Reviews of Modern Physics*, vol. 23, no. 4, p. 287, Oct. 1951.

[14] H. Huang, L. Tsang, A. Colliander, and S. H. Yueh, "Propagation of waves in randomly distributed cylinders using three-dimensional vector cylindrical wave expansions in foldy–lax equations," *IEEE Journal on Multiscale and Multiphysics Computational Techniques*, vol. 4, pp. 214–226, Dec. 2019.

[15] L. Tsang, J. A. Kong, and R. T. Shin, "Theory of microwave remote sensing," 1985.

[16] D. Andreuccetti, "An Internet resource for the calculation of the dielectric properties of body tissues in the frequency range 10 Hz-100 GHz," *http://niremf. ifac. cnr. it/tissprop/*, 2012.

[17] Y. Saad and M. H. Schultz, "Gmres: A generalized minimal residual algorithm for solving nonsymmetric linear systems," *SIAM Journal on scientific and statistical computing*, vol. 7, no. 3, pp. 856–869, July 1986.

[18] K. Zhao, M. N. Vouvakis, and J.-F. Lee, "The adaptive cross approximation algorithm for accelerated method of moments computations of emc problems," *IEEE transactions on electromagnetic compatibility*, vol. 47, no. 4, pp. 763–773, Nov. 2005.

[19] J. Shaeffer, "Low rank matrix algebra for the method of moments." *Applied Computational Electromagnetics Society Journal*, vol. 33, no. 10, Oct. 2018.

[20] G. Burger, H.-D. Bruns, and H. Singer, "Advanced method of moments based on iterative equation system solvers," in *IEEE 1997, EMC, Austin Style. IEEE 1997 International Symposium on Electromagnetic Compatibility. Symposium Record (Cat. No. 97CH36113)*. IEEE, 1997, pp. 236–241.